J. Fluid Mech. (2014), *vol.* 751, *pp.* 663–684.
doi:10.1017/jfm.2014.296

Response of a stratified boundary layer on a tilted wall to surface undulations

Pierre-Yves Passaggia[1,2], Patrice Meunier[1,†] and Stéphane Le Dizès[1]

[1]Aix Marseille Université, CNRS, Centrale Marseille, IRPHE UMR 7342, 13384, Marseille, France
[2]ONERA, the French Aerospace lab F-92322 Châtillon CEDEX, France

(Received 28 October 2013; revised 3 April 2014; accepted 22 May 2014)

The structure of a stratified boundary layer over a tilted bottom with a small streamwise undulation is studied theoretically and numerically. We show that the tilt of the boundary can induce strong density variations and wall-transverse velocities in the critical layer when the frequency of the forcing by the topography $kU(z_c)$ is equal to the transverse Brunt–Väisälä frequency $N \sin \alpha$ (N being the vertical Brunt–Väisälä frequency). The viscous solution in the critical layer, obtained and compared with direct numerical simulation results, is in good agreement for both the scaling and the spatial structure. The amplitude of the transverse velocity response is also shown to exhibit quasi-resonance peaks when the stratification strength is varied.

Key words: boundary layers, stratified flows, topographic effects

1. Introduction

Stratified boundary layer flows occur in both the ocean and the atmosphere when a tidal current or a nocturnal wind develops along a surface. The topology of these surfaces is generally complex and in the case of slopes, tilted with respect to the stratification. A natural approach to account for small amplitude topology is to consider a corrugated surface. For instance, these surfaces are representative of ocean bottoms such as seamounts where strong flow acceleration along the slopes has been reported in Genin *et al.* (1986). Sand waves formation, merely found along shallow continental slopes, are also a representative configuration (Besio *et al.* 2004). In the present work, we show that a free stream in a stratified medium on a tilted corrugated surface generates a strong transverse flow by a subtle interplay of stratification and shear.

Stratified boundary layer flows have mainly been studied on flat horizontal surfaces. Numerous works exist in the atmospheric context (see Garratt 1992). More recently, Mahrt (2014) reviewed the characteristics of the stably stratified atmospheric boundary layer. Corrugated surfaces have often been used to facilitate boundary layer transitions. There is an important literature on the receptivity of boundary layers for its possible applications to aeronautics (see for instance Saric, Reed & Kerschen 2002). In the atmospheric context, most works were motivated by understanding the effect of topography (e.g. Jackson & Hunt 1975; Taylor, Mason & Bradley 1987; Gong, Taylor

† Email address for correspondence: meunier@irphe.univ-mrs.fr

& Dornbrack 1996; Athanassiadou & Castro 2001), and vegetation (e.g. Finnigan, Shaw & Patton 2009) on boundary layer turbulence characteristics. The influence of a stable stratification has also been considered in the experimental works of Ohya (2001), Ohya & Uchida (2008). On the theoretical side, Thorpe (1992) has derived the structure of the lee internal waves generated by an undulated topography over a sloping bottom, in the presence of stratification and rotation. This structure has been observed numerically by MacCready & Pawlak (2001) over a sinusoidal topography but also over a solitary hill. Finally, we mention the recent works of Wu & Zhang (2008*a*,*b*) who analysed the development of a viscous instability wave and its interaction with a bump in a stratified boundary layer using the triple-deck framework (Sykes 1978). The effect of a slope has also been considered in a few field studies (Park & Park 2006; Nadeau *et al.* 2013) but we are not aware of any fundamental study in a controlled experimental framework.

When the surface is flat but inclined, we know that the deformation of the isopycnal near the boundary is the source of a flow along the slope which has been studied by Garrett, MacCready & Rhines (1993). Candelier, Le Dizès & Millet (2012) have recently shown that an inviscid instability, different from the inflectional instability, may also be active. This instability involves a phenomenon of over-reflection (Acheson 1976; Lindzen & Barker 1985) between the boundary and a critical point where the phase velocity matches the mean-flow velocity. It is very similar to the instability observed around a rotating cylinder (Riedinger, Le Dizès & Meunier 2011). In the present work, this instability, as well as the viscous boundary layer instability are not considered. We therefore assume that either the flow is stable (this will be the situation for our numerical simulations) or the forced response described below is not destroyed by these instabilities. We consider a small sinusoidal undulation with a fixed wavenumber. We are going to show that the wave generated by this undulation may exhibit a singular structure due to the presence of a critical point singularity.

This very thin structure is located within the boundary layer, with a large amplitude, even for small amplitudes undulations, which is very likely to be an important source of mixing and transport for ocean and atmospheric flows over slopes.

The paper is organized as follows. In § 2, we introduce the framework with the flow configuration and the numerical procedure. In § 3, we first provide numerical results. These results are then interpreted using an asymptotical analysis for large Reynolds numbers and small undulation amplitudes which leads to an expression for the maximum transverse velocity. The dependence of this expression on the Froude number and the undulation wavenumber is further analysed using a small Froude number description. Details of the analysis are given in appendix A. Section 4 provides a brief summary of the results and tentative applications to oceanic currents and atmospheric boundary layers.

2. Problem formulation

2.1. *Flow configuration*

We consider a boundary layer flow in a stratified fluid on a sinusoidally deformed tilted wall, as shown in figure 1. The wall is globally tilted in the cross-stream direction such that the z^*-axis of the (x^*, y^*, z^*) frame attached to the wall makes an angle α with respect to the Z^*-direction of stratification. The tilted frame of reference

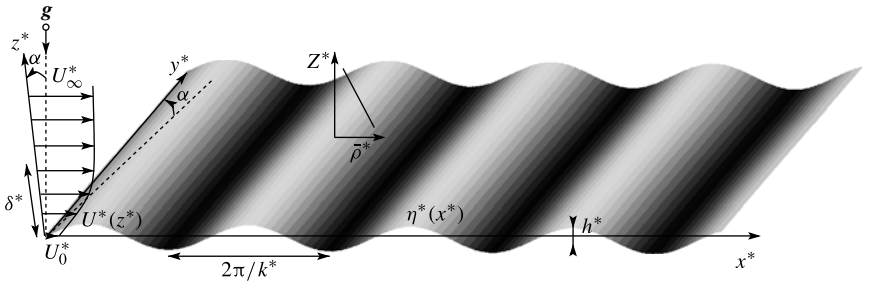

FIGURE 1. Sketch of the flow geometry.

is obtained from the horizontal/vertical coordinates (X^*, Y^*, Z^*) using the change of variables:

$$x^* = X^*, \quad y^* = Y^* \cos(\alpha) + Z^* \sin(\alpha) \quad \text{and} \quad z^* = Z^* \cos(\alpha) - Y^* \sin(\alpha). \tag{2.1a–c}$$

The inlet flow is assumed to be a typical tanh boundary layer flow of thickness δ^* and free stream velocity U^*_∞:

$$\boldsymbol{U}^* = U^*_\infty \tanh\left(\frac{z^* + z^*_0}{\delta^*}\right) \boldsymbol{e_x}. \tag{2.2}$$

A small penetration length z^*_0 has been introduced to allow the flow to slide on the boundary with a velocity $U^*_0 = U^*_\infty \tanh(z^*_0/\delta^*)$. This boundary condition mimics the condition obtained on the top of a viscous sublayer where roughness or small scale inhomogeneities could be present. It is the simplest way to model the flow over a canopy.

The fluid is assumed stably stratified along the vertical Z^* direction with a constant buoyancy frequency

$$N^* = \sqrt{-(g/\rho^*_0)(\partial \bar{\rho}^*/\partial Z^*)}, \tag{2.3}$$

where g is gravity.

The boundary is defined by the two-dimensional surface

$$z^* = \eta^*(x^*) = h^* \sin(k^* x^*) \tag{2.4}$$

where h^* and k^* correspond to the amplitude and wavenumber of the topography, respectively.

The flow is governed by the Navier–Stokes equations under the Boussinesq approximation, the incompressibility condition and the advection–diffusion equation for the density, that is,

$$\frac{\mathrm{D}\boldsymbol{u}^*}{\mathrm{D}t} = -\frac{\boldsymbol{\nabla} p^*}{\rho^*_0} - \frac{\rho^*}{\rho^*_0} g \boldsymbol{e_Z} + \nu \Delta \boldsymbol{u}^*, \tag{2.5a}$$

$$\boldsymbol{\nabla} \cdot \boldsymbol{u}^* = 0, \tag{2.5b}$$

$$\frac{\mathrm{D}\rho^*}{\mathrm{D}t} = \kappa \Delta \rho^*, \tag{2.5c}$$

where ν and κ are the kinematic viscosity and the thermal diffusivity, respectively. It satisfies the following boundary conditions at the wall

$$\boldsymbol{u}^*|_{z^*=\eta^*} = U_0^* \boldsymbol{t}; \quad \nabla\rho \cdot \boldsymbol{n}|_{z^*=\eta^*} = 0, \tag{2.6a,b}$$

where $\boldsymbol{t}$ and $\boldsymbol{n}$ are the wall tangent and normal vectors, respectively. Far from the wall ($z^* \to \infty$), the velocity and density fields are assumed to satisfy

$$\boldsymbol{u}^* \sim U_\infty^* \boldsymbol{e_x}; \quad \rho^* \sim \bar{\rho}^* = \rho_0^* \left(1 - (z^* \cos\alpha + y^* \sin\alpha) N^{*2}/g\right). \tag{2.7a,b}$$

In the following, we non-dimensionalize all the variables using δ^*, U_∞^* and ρ_0^*, and denote these variables without the star. The problem is characterized by six non-dimensional parameters

$$Re = \frac{U_\infty^* \delta^*}{\nu}, \quad F = \frac{U_\infty^*}{N^* \delta^*}, \quad \alpha, \quad h = h^*/\delta^*,$$
$$k = k^* \delta^*, \quad Pr = \frac{\nu}{\kappa}, \quad U_0 = \frac{U_0^*}{U_\infty^*}. \tag{2.8a–g}$$

We are interested in the configurations where Re is large and h is small. We also implicitly assume that the boundary layer flow on the undeformed wall is stable. This means that the Reynolds number is below the critical Reynolds number for the appearance of unstable Tollmien–Schlichting modes and unstable radiative modes.

2.2. *Numerical procedure*

Since the inlet flow is two-dimensional, we can assume that the flow remains two-dimensional downstream that is independent of the cross-stream variable y. For most numerical simulations, the numerical computational domain is taken from $x = -7.5$ to 52.5 and from $z = \eta(x)$ to $H = 18$. However, the boundary deformations only extend from $x = 0$ to $x = 42.5$, as shown in figure 2(*b*). The infinite flow domain is transformed into a Cartesian one using the mapping $\bar{x} = x$, $\bar{z} = z - \eta(x)$, the barred coordinates being the computational ones. The numerical procedure is detailed in Marquillie & Ehrenstein (2002) and proved to accurately predict the phenomenon of transitional boundary layers (Marquillie & Ehrenstein 2003; Passaggia, Leweke & Ehrenstein 2012). Since the mapping transformation requires $\eta(x)$ to be twice differentiable, the lower boundary has been smoothed in the vicinity of $x = 0$ and $x = 42.5$ using regularization procedures based on convolution between the wall function $\eta(x)$ and a third order polynomial kernel. The inlet boundary condition is given by the boundary layer profile (2.2) and $\rho = \bar{\rho}$.

Following the numerical procedure of Marquillie & Ehrenstein (2003), a convective condition has been implemented at the outflow for all velocity components $\boldsymbol{u}$ and the density ρ such that

$$\frac{\partial \boldsymbol{u}}{\partial t} = U_c \frac{\partial \boldsymbol{u}}{\partial x}, \quad \frac{\partial \rho}{\partial t} = U_c \frac{\partial \rho}{\partial x}, \quad U_c = \frac{1}{z^\dagger} \int_0^{z^\dagger} u_x(42.5, z) \mathrm{d}z \tag{2.9a,b}$$

where $z^\dagger$ was chosen for the streamwise velocity $u_x(42.5, z)$ to be equal to 0.5, which is the uniform flow at infinity (Marquillie & Ehrenstein 2002).

When addressing the question of stratified incompressible flows in a finite computational domain, sponge layers appear to be mandatory to avoid spurious

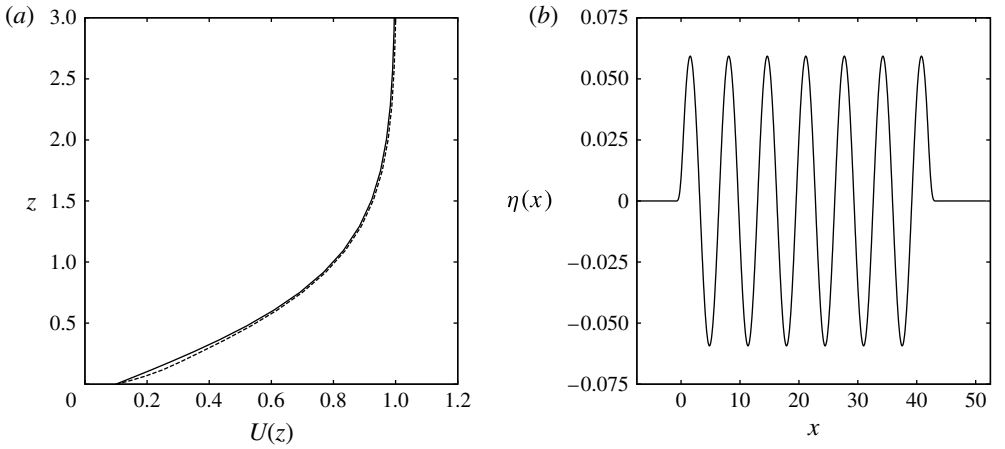

FIGURE 2. (*a*) Velocity profiles at the inlet (solid line) and at the summit of an oscillation $x = 30.3$ (dashed line) for $Re = 593$ and $h = 0.06$. (*b*) Graph of the lower boundary $\eta(x)$ of the small computational domain at $h = 0.06$.

modes arising from a finite computational domain together with boundary conditions (2.9). In the present case, the sponge layers consist of hyperbolic tangent functions which smoothly cancel the advection term of the equation for the density ρ. In the present study, they are present close to the inlet for $-7.5 < x < -4.5$ and far from the wall for $15 < z < 18$, which has proved to be appropriate to achieve convergence in all cases considered. The present calculations have been performed calculating first the vertical flow solution at $\alpha = 90°$. Restarting from this solution, the tilted flow solution has been computed until convergence of the time marching algorithm up to 10^{-6} of the solution vector.

Most numerical simulations are carried out in the computational domain defined above. The Reynolds number Re is varied from 60 to 1200, the Froude number F from 0.95 to 1.15, the tilt angle α from 15 to 75° and the non-dimensional wavenumber k from 0.85 to 1.25. Different computational domains have also been considered in order to treat more extreme values of k and document the behaviour of the solution for small and large Froude numbers. In all the simulations, the sliding velocity is fixed to $U_0 = 0.1$ and the Prandtl number Pr is equal to 0.7 in order to simulate the thermal diffusion of air.

3. Structure of a stratified tilted boundary layer

3.1. *Numerical results*

In this section, we present the typical characteristics of the flow obtained in the numerical simulations. Figure 3 shows the transverse component of velocity in a plane normal to the bottom. The field contains a series of alternate lobes clearly separated from the bottom with the same wavelength as the undulated topography, but in phase quadrature. Above these lobes, the velocity presents almost vertical bands of weak amplitude, characteristic of lee waves created by an undulated topography.

Figure 4 shows the profile of velocity and density at the altitude of the lobes $z_c = 0.75$. It is striking to see that the transverse velocity (dashed line) is five times larger than the normal velocity although the sliding velocity along the topography generates

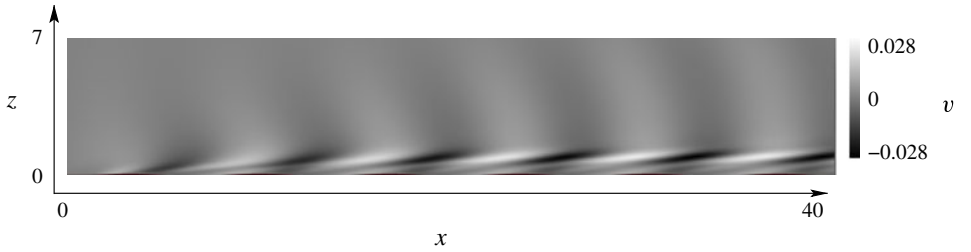

FIGURE 3. The two-dimensional field of the transverse velocity $v(x, z)$ for $h = 0.06$, $F = 1.046$, $k = 1.041$, $Re = 1186$ and $\alpha = \pi/4$.

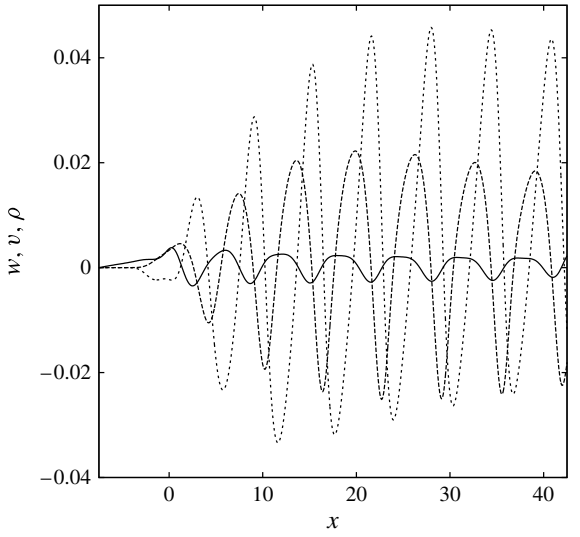

FIGURE 4. Streamwise profile of the normal velocity w (solid line), transverse velocity v (dashed line) and density ρ (dotted line) at $z_c = 0.75$. Here $Re = 593$, $F = 1.046$, $k = 1.041$, $\alpha = \pi/4$ and $h = 0.06$.

only a normal velocity. The density also exhibits large sinusoidal perturbations which are 10 times larger than the normal velocity. These oscillations start at the beginning of the undulated topography ($x = 0$), grow during a transient stage of approximately three to four undulations and then saturate.

The altitude z_c of the divergence of v and ρ has been measured for various parameters. As shown in figure 5, it is independent of the height of the topography and very weakly dependent on the Reynolds number. However, it clearly depends on the Froude number, the tilt angle and the wavenumber. This critical altitude z_c corresponds to the position where the normal component of the wavevector diverges. Indeed, in the tilted frame of reference (x, y, z), a lee wave with wavevector $\boldsymbol{k} = (k, 0, m)$ has a frequency given by the linear dispersion relation:

$$\omega = kU \pm \frac{1}{F}\frac{\|\boldsymbol{k}_{Hor.}\|}{\|\boldsymbol{k}\|} = kU \pm \frac{\sqrt{k^2 + m^2 \sin^2\alpha}}{F\sqrt{m^2 + k^2}}. \tag{3.1}$$

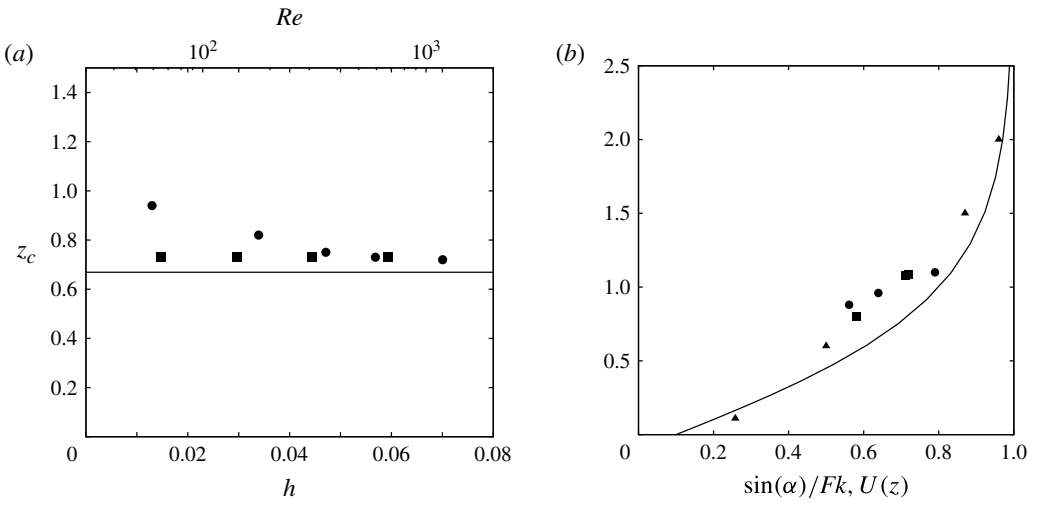

FIGURE 5. Position of the critical layer z_c measured at the maximum of v. In (a), z_c is plotted as a function of h (■) and as a function of Re (●) for $F = 1.046$, $\alpha = \pi/4$ and $k = 1.041$. In (b), z_c is plotted as a function of $\sin\alpha/(kF)$ for $Re = 593$ and $h = 0.06$. In (b), symbols correspond to F (■), k (●) and α (▲); the solid line corresponds to the velocity profile $U(z_c)$.

The variation of U with altitude bends the waves such that the normal wavenumber m varies with altitude in order for the wave to be stationary. Assuming $\omega = 0$ in (3.1) leads to

$$m^2 = k^2 \frac{1 - k^2U^2F^2}{k^2U^2F^2 - \sin^2\alpha} \tag{3.2}$$

which diverges for

$$U(z_c) = \frac{\sin\alpha}{Fk}. \tag{3.3}$$

This criterion defines a critical altitude z_c which is plotted in figure 5 as a solid line. It is reasonably close to the altitude where v and ρ attain their maxima. This indicates that the strong variations in v and ρ come from the divergence of the wavenumber m. However, this analysis is only valid when the wavelength of the lee wave is much smaller than the thickness of the boundary layer. In the next section, the analysis is extended for any wavelength, but for the case of small undulation height h.

3.2. *Expansion for small wall oscillation amplitudes*

The structure of the boundary layer can be described asymptotically for a small amplitude h of the topography and a large Reynolds number. The solution is decomposed into a base flow $(\boldsymbol{U}_b, \rho_b, p_b)$ and a small perturbation $(\boldsymbol{u}, \rho, p)$ which is postulated as a spatial Fourier mode of wavenumber k and amplitude h:

$$(\boldsymbol{u}, \rho, p) = \tfrac{1}{2}hk(\tilde{\boldsymbol{u}}, U_\infty^2/(\delta g)\tilde{\rho}, \tilde{p})\mathrm{e}^{\mathrm{i}kx} + \text{c.c.} \tag{3.4}$$

The base flow corresponds to the solution on a flat but inclined wall. In the limit of large Reynolds numbers, it remains close to the inlet flow as long as we consider

streamwise location to be small compared to the viscous diffusion scale $x_v = O(Re)$. The normal flow correction induced by this weak diffusion process is $O(1/Re)$. A weak cross-flow is also present as soon as the wall is inclined. This flow is associated with density correction generated by the inclination of the isopycnals with respect to the boundary. To cancel the normal density gradient at the wall, a density correction and a weak cross-flow is created very close to the wall. This boundary layer flow was analysed in detail in Garrett *et al.* (1993). Neither the cross-flow, nor the density correction has an impact far from the boundary.

The equations satisfied by the amplitude of the Fourier mode can be obtained by linearizing the governing equations (2.5) around the base flow solution. We get to first order in h:

$$\mathrm{i}kU\tilde{u} + \tilde{w}U' = -\mathrm{i}k\tilde{p} + \frac{1}{Re}\tilde{\Delta}\tilde{u}, \tag{3.5a}$$

$$\mathrm{i}kU\tilde{v} = -\sin\alpha\,\tilde{\rho} + \frac{1}{Re}\tilde{\Delta}\tilde{v}, \tag{3.5b}$$

$$\mathrm{i}kU\tilde{w} = -\cos\alpha\,\tilde{\rho} - \frac{\partial\tilde{p}}{\partial z} + \frac{1}{Re}\tilde{\Delta}\tilde{w}, \tag{3.5c}$$

$$\mathrm{i}kU\tilde{\rho} = \frac{\tilde{w}\cos\alpha + \tilde{v}\sin\alpha}{F^2} + \frac{1}{RePr}\tilde{\Delta}\tilde{\rho}, \tag{3.5d}$$

$$\mathrm{i}k\tilde{u} + \frac{\partial\tilde{w}}{\partial z} = 0, \tag{3.5e}$$

where $\tilde{\Delta} = \partial_z^2 - k^2$. Note that we have artificially kept small diffusion terms but neglected the base flow corrections mentioned above. We will see below that the diffusion terms do become important close to the critical layer singularity while the base flow corrections remain negligible. The boundary conditions obtained from (2.6) are, to leading order in h,

$$\tilde{u}(z=0) = \mathrm{i}(1-U_0^2); \quad \tilde{v}(z=0) = 0; \quad \tilde{w}(z=0) = U_0; \quad \partial_z\tilde{\rho}(z=0) = 0. \tag{3.6a–d}$$

Far from the wall, as z goes to infinity, the perturbation should either vanish or be an outgoing wave.

In the inviscid regions where the diffusion terms are negligible, we get the following equations from (3.5) as $Re \to \infty$:

$$\tilde{p} = \frac{U}{\mathrm{i}k}\frac{\partial\tilde{w}}{\partial z} - \tilde{w}\frac{U'}{\mathrm{i}k}, \quad \tilde{\rho} = \frac{\mathrm{i}kU\tilde{w}\cos\alpha}{\sin^2\alpha - k^2U^2F^2}, \quad \tilde{v} = \frac{\tilde{w}\sin\alpha\cos\alpha}{\sin^2\alpha - k^2U^2F^2}. \tag{3.7a–c}$$

Substituting these expressions in (3.5c) leads to a single differential equation for the wall-normal velocity

$$\tilde{w}'' - \frac{U''}{U}\tilde{w} - k^2\frac{1-k^2U^2F^2}{\sin^2\alpha - k^2U^2F^2}\tilde{w} = 0. \tag{3.8}$$

This equation reduces to the well-known Taylor–Goldstein equation for the tilt angle $\alpha = 0$. It is clear that the last term of this equation is singular at the point z_c where $kU(z_c)F = \sin\alpha$. Such a singularity corresponds to a so-called critical point. Viscous effects have to be re-introduced to smooth the singularity. The singularity is weak as an expansion of the coefficients in powers of $z - z_c$ indicates that $\tilde{w}$ expands as

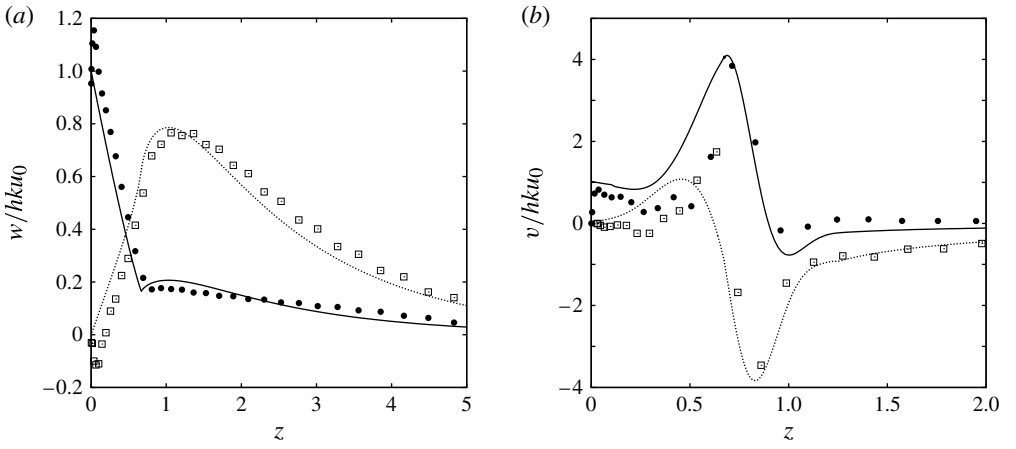

FIGURE 6. Normal profile of (a) normal velocity w and (b) transverse velocity v. The profiles are measured on the lee side of the undulations at $x = 7\pi/k$ (•, solid line) and on the bottom of the undulation at $x = 7.5\pi/k$ (□, dashed line). Symbols correspond to numerical simulations and lines to theoretical predictions. Here $h = 0.03$, $F = 1.046$, $k = 1.041$, $Re = 1423$ and $\alpha = \pi/4$.

$\tilde{w} \sim a^{\pm} + a^{\pm}\kappa(z - z_c)\log|z - z_c| + b^{\pm}(z - z_c)$ with $\kappa = k\cos^2\alpha/(2\sin\alpha FU'(z_c))$ on either side of z_c. This critical point singularity is the classical singularity found in the stability of homogeneous shear flows (Lin 1955). Note that it is different from that of stratified shear flows over horizontal walls. The viscous smoothing can be used to get the adequate jumps conditions across the critical point:

$$a^+ = a^- = \tilde{w}_c; \quad b^+ = b^- + \mathrm{i}\pi\kappa\tilde{w}_c. \tag{3.9a,b}$$

These jump conditions can also be obtained from the property that the inviscid solution remains asymptotically valid in any contour that avoids the critical point in the lower complex half-plane, a condition which is derived from the asymptotic behaviour of the viscous solutions near z_c or from the condition of causality (see Lin 1955, for more explanation on this issue). These conditions tell us that the solution is continuous at z_c but its derivative exhibits a jump.

Using these jump conditions, (3.8) with the boundary conditions prescribed above can easily be solved using conventional integration software; we obtain the solution plotted in figure 6(a). Note that the jump of $\tilde{w}'$ at z_c is clearly visible on the real part of the signal. In this figure, the real part and the imaginary part of the solution are compared to the numerical signals of the normal velocity at the lee side ($kx = 7\pi$) and at the bottom ($kx = 7.5\pi$) of the undulation, respectively. We can note that, except in the wall boundary layer, there is good qualitative agreement between the two results.

The inviscid approximation of the normal velocity is continuous at z_c. By contrast, (3.7) and (3.5b) demonstrate that both the transverse velocity v and ρ diverge at $z = z_c$. This behaviour is in agreement with the very large amplitudes of the transverse velocity and of the density observed in the numerics. In order to determine the maximum amplitude of these two quantities, we have to solve the viscous critical layer. This is done in the next section.

3.3. *Viscous critical layer analysis*

The analysis of viscous critical layers is a classical problem which is described in several textbooks (see for instance Drazin & Reid 1981). A very similar analysis has also been done in the context of vortices in Boulanger, Meunier & Le Dizès (2007). We provide here the main steps of the analysis.

In the viscous critical layer, the structure of the solution is obtained by introducing a new local viscous scale $\hat{z} = (z - z_c)Re^{1/3}$. The form of the solution can be obtained by expanding the non-viscous solution close to the critical point. We find that the solution has to take the form

$$\tilde{u} = \hat{u}(\hat{z}) + \log(Re)\hat{u}_s, \tag{3.10a}$$

$$\tilde{v} = \hat{v}(\hat{z})Re^{1/3}, \tag{3.10b}$$

$$\tilde{w} = \tilde{w}_c + \hat{w}(\hat{z})Re^{-1/3} + Re^{-1/3}\log(Re)\hat{w}_s\hat{z}, \tag{3.10c}$$

$$\tilde{\rho} = \hat{\rho}(\hat{z})Re^{1/3}, \tag{3.10d}$$

$$\tilde{p} = \hat{p}(\hat{z}) + \log(Re)\hat{p}_s. \tag{3.10e}$$

Note that the $\log(Re)$ terms come from the special behaviour of the normal velocity close to the critical point. Expanding the base flow velocity as

$$U(z) \sim U(z_c) + U'(z_c)(z - z_c) = \frac{\sin\alpha}{kF} + U_c'\hat{z}Re^{-1/3}, \tag{3.11}$$

the system (3.5) reduces to

$$\mathrm{i}kU_c(\hat{u} + \log(Re)\hat{u}_s) + \hat{w}_cU_c' = \mathrm{i}k(\hat{p} + \log(Re)\hat{p}_s), \tag{3.12a}$$

$$\mathrm{i}kU_c\tilde{w}_c = -\cos\alpha\hat{\rho}Re^{1/3} - \frac{\partial\hat{p}}{\partial\hat{z}}Re^{1/3}, \tag{3.12b}$$

$$\frac{\mathrm{i}\sin\alpha\hat{v}Re^{1/3}}{F} + \mathrm{i}kU_c'\hat{z}\hat{v} = -\sin\alpha\hat{\rho}Re^{1/3} + \hat{v}'', \tag{3.12c}$$

$$\frac{\mathrm{i}\sin\alpha\hat{\rho}Re^{1/3}}{F} + \mathrm{i}kU_c'\hat{z}\hat{\rho} = \frac{(\hat{v}\sin\alpha Re^{1/3} + \cos\alpha\tilde{w}_c)}{F^2} + \frac{1}{Pr}\hat{\rho}'', \tag{3.12d}$$

$$\mathrm{i}k(\hat{u} + \log(Re)\hat{u}_s) = -\frac{\partial\hat{w}}{\partial\tilde{z}} - \log(Re)\hat{w}_s. \tag{3.12e}$$

To leading order in $Re^{-1/3}$, (3.12*c*) and (3.12*d*) both indicate that $\hat{\rho} = -\mathrm{i}\hat{v}/F$. Introducing this result in (3.12*c*)–iF(3.12*d*) leads to a differential equation, to first order, for the transverse velocity $\hat{v}$:

$$2\mathrm{i}kU_c'\hat{z}\hat{v} = \left(1 + \frac{1}{Pr}\right)\hat{v}'' + \frac{\mathrm{i}\tilde{w}_c\cos\alpha}{F}. \tag{3.13}$$

The function $\hat{p}(\hat{z})$ can then be deduced from (3.12*b*), which then gives $\hat{u}(\hat{z})$ from (3.12*a*) and $\hat{w}(\hat{z})$ from (3.12*e*) provided that $\hat{w}_s = -\mathrm{i}k\hat{u}_s = -\mathrm{i}k\hat{p}_s/U_c$ (such that the log terms disappear). The matching with the outer solution gives $\hat{w}_s = -\tilde{w}_c\kappa/3$.

Equation (3.13) is an inhomogeneous Airy equation. In order to match an inviscid solution in the outer region, the solution must behave as $\hat{z}^{-1}$ for large $|\hat{z}|$. As shown by Drazin & Reid (1981), the solution which satisfies this condition is a generalized Airy function $B_k(K\hat{z}, 1)$. It can also be expressed in terms of Scorer's function $\mathrm{Hi}(z)$

(Abramowitz & Stegun 1965, p. 448) which satisfies $\mathrm{Hi}''(z) - z\mathrm{Hi}(z) = 1/\pi$ as follows

$$\hat{v}(\hat{z}) = \frac{\mathrm{i}\tilde{w}_c \pi \cos\alpha}{\xi^2 F(1+1/Pr)} \mathrm{Hi}(-\mathrm{i}\xi\hat{z}). \tag{3.14}$$

with $\xi = \left(2kU_c'/(1+1/Pr)\right)^{1/3}$. A composite expression for the transverse velocity can be obtained from the non-viscous solution $\tilde{v}$ (3.7) and the critical layer solution $\hat{v}$ (3.14), namely

$$v(z) = \frac{\tilde{v}(z)\hat{v}((z-z_c)Re^{1/3})2kU_c'F(z-z_c)}{\tilde{w}_c \cos\alpha}. \tag{3.15}$$

This expression is plotted in figure 6(*b*) as a solid line for the real part and a dashed line for the imaginary part. We can see that these two profiles are comparable to the numerical results obtained at the lee side and at the bottom of the undulation. A small shift is nevertheless observed which might come from higher order corrections.

The maximum of the transverse velocity v_{max} over the whole field can now be predicted from the maximum of the Scorer's function $\mathrm{Hi}_{max} = \mathrm{Hi}(0) \approx 0.41$. In terms of the initial variables, we get

$$v_{max} = \frac{hkU_0 Re^{1/3}}{(1+1/Pr)^{1/3}} V(F, k, \alpha, U_0), \tag{3.16}$$

where

$$V(F, k, \alpha, U_0) = \frac{\mathrm{Hi}_{max}\pi\cos\alpha}{F(2k)^{2/3}(1-\sin^2\alpha/(kF)^2)^{2/3}} \Delta_c \tag{3.17}$$

and

$$\Delta_c = \left|\frac{\tilde{w}_c}{\tilde{w}_0}\right|. \tag{3.18}$$

In the above expression, we have used the relation $U_c' = 1 - \sin^2\alpha/(kF)^2$ and the definition $\tilde{w}_0 = \tilde{w}(z=0) = U_0$.

The function v_{max} is plotted and compared to the numerical results in figure 7. It clearly shows that the amplitude of the critical layer is linear in h with an excellent quantitative prediction of the amplitude. The amplitude also scales as $Re^{1/3}$ although the lowest Reynolds number is slightly above the theoretical prediction. This is possibly due to the modification of the mean profile by viscous effects in the numerics or to the fact that the critical layer becomes so large that it interacts with the near wall boundary layer flow.

The thickness ζ of the critical layer has also been measured in the numerics as the distance between the maximum and the minimum of v in the shear profile (at $kx = 7.5\pi$). Note that each value of the thickness ζ was rescaled with the local thickness of the boundary layer, for each value of Re. The data are plotted in figure 8. We observe that the thickness does decrease as $Re^{-1/3}$ and is in good agreement with the theory although it is 20 % below the prediction.

3.4. *Dependence with respect to the Froude number and the undulation wavenumber*

In this section, we use the theory to discuss the dependence of v_{max} with respect to the Froude number and the undulation wavenumber.

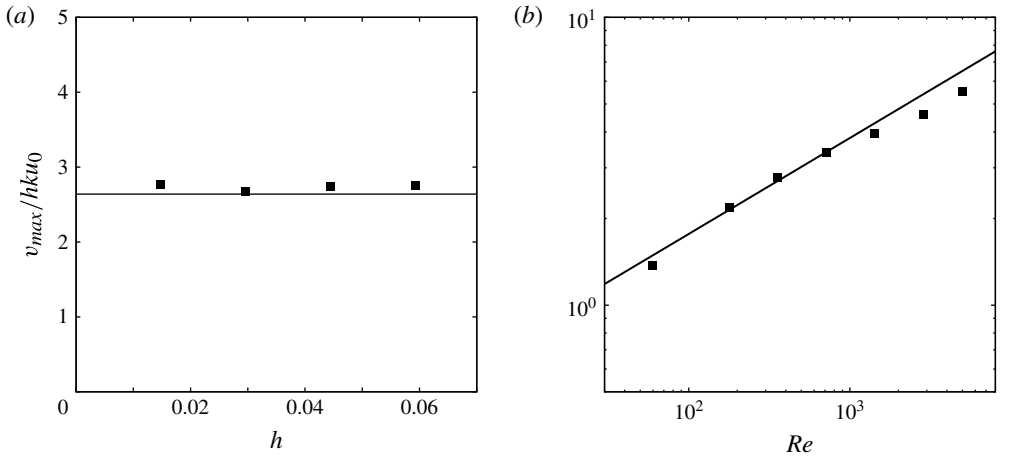

FIGURE 7. Renormalized amplitude of the critical layer $v_{max}/(hkU_0)$ as a function of (a) the height of the hills h and (b) the Reynolds number. Numerical values (■) obtained at $x = 7.5\pi/k$ are compared with the theoretical prediction (solid line) given by (3.16). Here $F = 1.046$, $k = 1.041$ and $\alpha = \pi/4$. In (a) $Re = 593$ and in (b) $h = 0.03$.

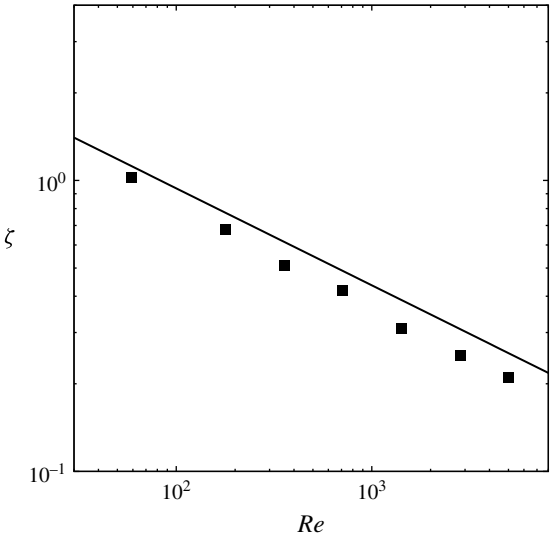

FIGURE 8. Thickness of the critical layer as a function of the Reynolds number measured on the lee side of a hill at $x = 7.5\pi/k$. The theoretical prediction (solid line) is compared to the numerical simulations (■); $h = 0.03$, $F = 1.046$, $k = 1.041$ and $\alpha = \pi/4$.

The contours of the function $V(F, k, \alpha, U_0)$ appearing in (3.16) are plotted in figure 9 for a small and a large tilt angle ($\alpha = \pi/60$ and $\alpha = \pi/6$). These plots show that V exhibits complex variation with respect to the parameters. Note in particular in figure 9(b) the discontinuous behaviour across the line $kF = 1$ and the peaky structure for small F close to the right frontier corresponding to $kF = \sin\alpha/U_0$. Large values of V are reached in two limits which can be analysed separately: (i) large F and kF

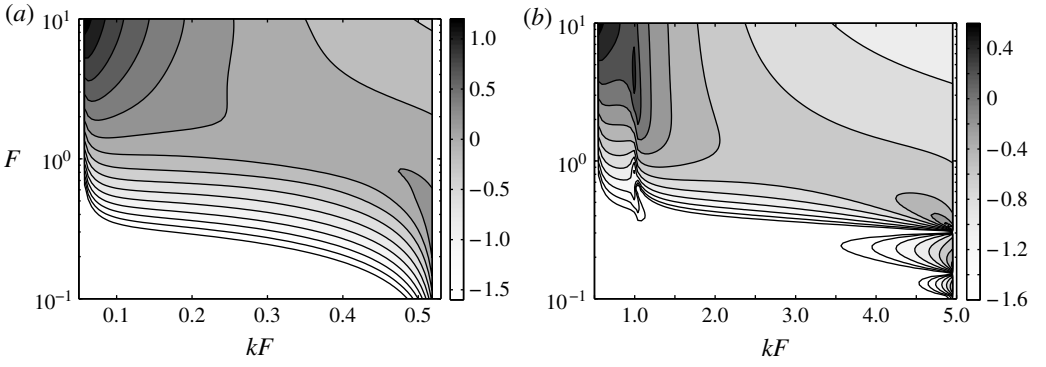

FIGURE 9. Contour levels of the function $\log_{10} V$ in the (kF, F) plane for $U_0 = 0.1$ and (*a*) $\alpha = \pi/60$ or (*b*) $\alpha = \pi/6$. The function V is defined for $\sin\alpha < kF < \sin\alpha/U_0$ only (condition of existence of a critical point).

close to $\sin\alpha$ (top left corners of figure 9), and (ii) small F and kF close to $\sin\alpha/U_0$ (bottom right corners of figure 9).

The first limit is the easier to analyse. For large F, the solution $\tilde{w}$ does indeed have a simple bulk approximation $\tilde{w}(z) \sim U(z)$. This approximation is valid up to the (large) altitude where the second term in (3.8) becomes of same order as the third term. The critical velocity is thus given by

$$\Delta_c = \left|\frac{\tilde{w}_c}{\tilde{w}_0}\right| \sim \frac{\sin\alpha}{kFU_0}, \quad \text{as } F \to \infty. \tag{3.19}$$

We can then deduce that

$$V \sim \frac{\mathrm{Hi}_{max}\,\pi\cos\alpha}{U_0 F^{1/3}(2\sin\alpha)^{2/3}(1-\sin^2\alpha/(kF)^2)^{2/3}} \quad \text{as } F \to \infty, \tag{3.20}$$

which tell us how v_{max} varies with respect to kF for large F. Figure 10 demonstrates that (3.19) provides a very good estimate of Δ_c as soon as F is larger than a few tens. In figure 10(*b*), we have also added values of Δ_c obtained from direct numerical simulation for $F = 10$, $Re = 593$ and $h = 0.12$. We can see that they follow the theoretical curve reasonably well.

The second limit is more involved due to the singular structure of the normal velocity $\tilde{w}(z)$ as $F \to 0$. In appendix A, we show how an approximation of the function Δ_c can be obtained using a WKBJ analysis. It is first shown that, when F is small, Δ_c is in general exponentially small. Large values of Δ_c are only obtained when $\sin\alpha/(kF)$ is very close to U_0, as expected from figure 9. This case corresponds to the limit (ii). In this limit, simple approximations are obtained for Δ_c:

$$\Delta_c = \frac{1}{X\sqrt{[\mathrm{K}_1(X)]^2 + \pi^2[\mathrm{I}_1(X)]^2}} \quad \text{when } kF < 1, \tag{3.21a}$$

$$\Delta_c = \frac{1}{X\sqrt{\left[\mathrm{K}_1(X) + \dfrac{\pi}{2\tan\Phi}\mathrm{I}_1(X)\right]^2 + \dfrac{\pi^2}{4}[\mathrm{I}_1(X)]^2}}, \quad \text{when } kF > 1, \tag{3.21b}$$

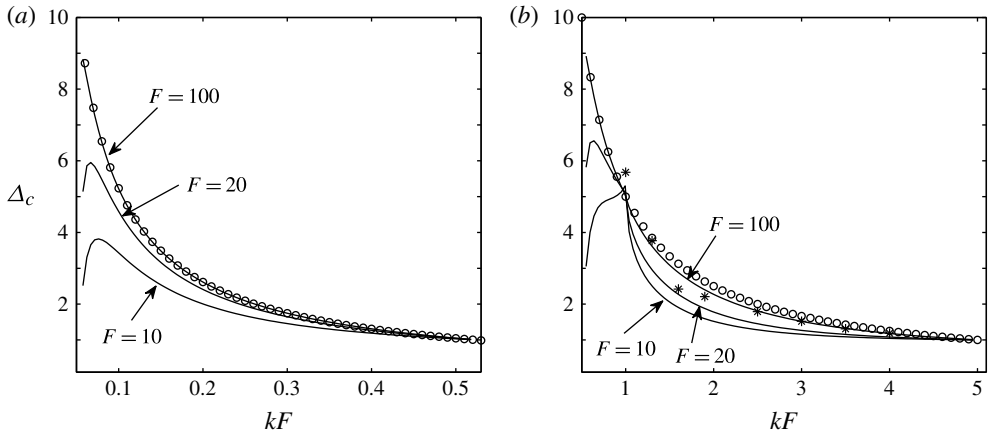

FIGURE 10. The function Δ_c versus kF for different values of F for (a) $\alpha = \pi/60$ and (b) $\alpha = \pi/6$. Solid lines denote numerically computed values; symbols denote values obtained from expression (3.19). The stars in (b) are estimates obtained from the direct numerical simulation for $F = 10$, $Re = 593$ and $h = 0.12$.

where I_1 and K_1 are modified Bessel functions and

$$\Phi = k \int_{z_c}^{z_\infty} \sqrt{\frac{1 - (kF)^2 U^2(z)}{(kF)^2 U^2(z) - \sin^2\alpha}}\, \mathrm{d}z, \tag{3.22a}$$

$$X = \frac{\cos\alpha}{(1 - U_0^2)F} \sqrt{2\left(1 - \frac{kFU_0}{\sin\alpha}\right)}. \tag{3.22b}$$

The approximation depends on the size of kF with respect to unity because the structure of $\tilde{w}$ changes when $kF > 1$. When $kF < 1$, the solution is oscillating up to infinity, whereas, when $kF > 1$ it becomes evanescent after the turning point z_∞ where $kFU(z_\infty) = 1$. The theoretical approximation is compared to the computed curve in figure 11. We can observe that it provides a good approximation even for F as large as unity. In figure 11(b), we have also plotted the values provided by the direct numerical simulation for $kF = 4.96$, $Re = 596$ and $h = 0.12$. Although the largest and smallest values of Δ_c are not recovered, we can observe that the oscillations of Δ_c as F varies are qualitatively reproduced.

The behaviour of Δ_c for $kF > 1$ is particularly interesting as it exhibits distinct peaks and valleys. A simple estimate of Φ can be obtained in the limit of small α:

$$\Phi \sim -\frac{\log(\alpha)}{F}. \tag{3.23}$$

The valleys correspond to the configurations where $\tan\Phi = 0$, that is $\Phi = n\pi$, $n = 1, 2, 3, \ldots$. For small α, they are therefore obtained for fixed values of F (for any k and U_0) given by

$$F_V^{(n)} = -\frac{\log(\alpha)}{n\pi}. \tag{3.24}$$

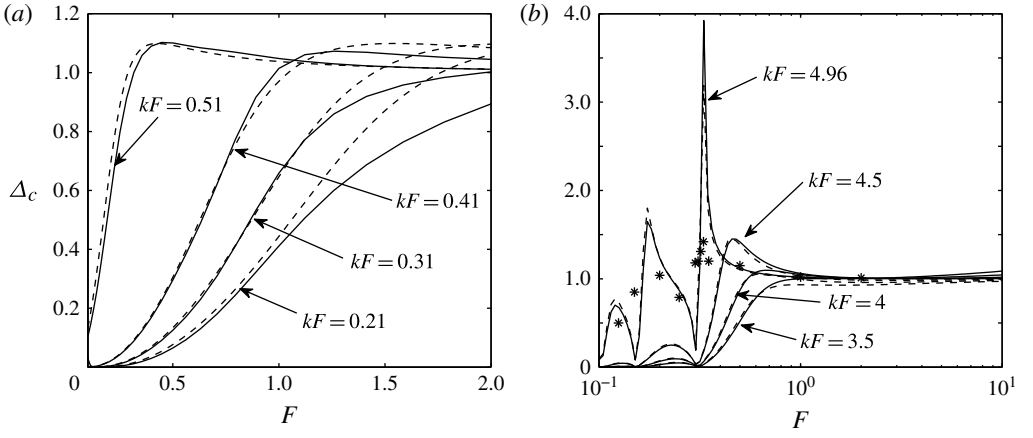

FIGURE 11. The function Δ_c versus F for different values of kF for (*a*) $\alpha = \pi/60$ and (*b*) $\alpha = \pi/6$. Solid lines denote numerically computed values; dashed lines denote values obtained from (3.21*a*,*b*). The stars in (*b*) are estimates obtained from the direct numerical simulation for $kF = 4.96$, $Re = 593$ and $h = 0.12$.

Present between each valley is a peak, which is reached (for small α) for

$$F_P^{(n)} = -\frac{\log(\alpha)}{n\pi - \arctan\left(\dfrac{\pi}{2}\dfrac{\mathrm{I}_1(X)}{\mathrm{K}_1(X)}\right)}. \tag{3.25}$$

These peaks are largest when X is smallest, that is when kF is closest to $\sin\alpha/U_0$. Their amplitude decreases as X increases. This means that for a fixed value of kF, the amplitude of the peak decreases as F decreases, as observed in figure 11.

In summary, when F is small, we have shown that Δ_c (and thus also v_{max}) reaches its largest values when kF is slightly below $\sin\alpha/U_0$, that is, when the critical point is close to the wall. When $kF > 1$, a phenomenon of resonance and anti-resonance is observed generating large fluctuations of Δ_c as F is varied. This phenomenon directly affects the maximum transverse velocity v_{max}, which is proportional to Δ_c (see (3.16) and (3.17)). For large F, we have seen that the largest values of v_{max} are obtained when kF is slightly above $\sin\alpha$, that is when the critical point is far away from the wall.

Note however that when F is of order one, V remains $O(1)$. In that case, all the corrugation wavenumbers k satisfying $(\sin\alpha)/F < k < (\sin\alpha)/(U_0F)$ are thus expected to give a large transverse flow response.

4. Conclusion

In this paper, we have presented some numerical and theoretical results on the internal waves generated by a sinusoidal topography on an inclined bottom. The velocity profile $U^*(z^*)$ has been chosen to be a hyperbolic tangent profile, with a sliding velocity at the bottom. The inclination of the bottom has been found to create a large transverse velocity at the distance to the wall where the frequency of the topographic forcing $k^*U^*(z)$ is equal to the transverse buoyancy frequency $N^*\sin\alpha$ (in dimensional units). We have shown that this large amplitude is associated

with a critical layer singularity of the inviscid solution. We have also shown that the solution can be regularized by performing a viscous critical layer analysis. An analytic solution has been obtained and found to be in good agreement with the numerical results. The maximum transverse velocity has been shown to be larger by a factor of $Re^{1/3}$, the normal velocity generated by the undulation at the wall. Interestingly, the transverse velocity has also been found to exhibit well-defined peaks associated with a quasi-resonance phenomenon for specific values of the Froude number, when kF is larger than one and close to $\sin\alpha/U_0$.

The analysis has been based on the hypothesis that the fluid slides on the boundary with a constant velocity. This sliding velocity guarantees that a non-negligible normal velocity is created by the undulations. This hypothesis implicitly assumes that the size of the undulations is larger than the viscous sublayer width. Note in particular that if the undulations were within the sublayer ($h \ll Re^{-1/3}$), the normal velocity would scale as $O(Re^{-1/3})$ and the maximum transverse velocity would then not be that large.

The present study demonstrates that the interplay between undulation and tilting could have a strong impact on the dynamics of stratified boundary layer flow. A small deformation on a weakly inclined bottom can generate a large transverse flow. This transverse flow is $O(Re^{1/3})$ larger than the sliding velocity and localized in a $O(Re^{-1/3})$ layer. For large Reynolds numbers, it therefore induces a strong transverse shear which may become unstable with respect to the Kelvin–Helmholtz instability. Such a mechanism has been observed in the dynamics of a tilted vortex (Boulanger, Meunier & Le Dizès 2008). We suspect that it could be active in the boundary layer.

Note also that nonlinear effects are expected to arrive first in the critical layer. In particular, the critical layer is expected to become nonlinear as soon as the amplitude of the transverse velocity reaches $Re^{-1/3}$. It would therefore be interesting to pursue the analysis in the nonlinear regime using the framework of the nonlinear critical layer theory (Benney & Bergeron 1969; Haberman 1972).

The present mechanism of mixing is expected to be in competition with the mixing induced by the boundary layer instabilities on a flat wall. At least two types of instability are expected to be present on a tilted wall for large Reynolds numbers: viscous boundary layer instability, associated with Tollmien–Schlichting modes (Wu & Zhang 2008*a*), and radiative instability which is inviscid in nature and present only if the wall is inclined (Candelier *et al.* 2012). The conditions for the appearance of these two instabilities in the parameter space (α, F, Re) are only partially known (Bai 2012) but both instabilities are expected to be present for the large Reynolds numbers of geophysical flows. It would thus be interesting to simulate a configuration where one of these instabilities is also present.

For very high Reynolds numbers, we expect the boundary layer to become turbulent. Yet, it is possible that the present mechanism could still be active in this regime. Indeed, a similar analysis can *a priori* be performed with a mean turbulent boundary layer profile and a turbulent eddy viscosity and it would lead to the same conclusion.

The phenomenon could then be present in real geophysical flows. For instance, taking values from the continental slope in Besio *et al.* (2004), the mean current flow velocity is 0.07 cm s^{-1}, the boundary layer thickness is estimated at 10 m, and for the mean Brunt–Väisälä frequency measured at $N = 0.024$ (van Haren & Howarth 2004), we obtain $F = 0.29$. For $U_0 = 0.1$ and a tilt angle close to $\alpha = \pi/90$ the present results tell us that all the corrugation wavelengths larger than 73 m will generate a response with a critical layer and therefore will be a source of transverse flow. Note that the wavelength of sand waves studied in Besio *et al.* (2004) appear to have a threshold close to 100 m and height between 1 m and 10 m, which is consistent with the present study.

For a stably stratified atmospheric boundary layer flow, if we take the values reported by Frehlich, Meillier & Jensen (2008), that is, a nocturnal wind of velocity 10 m s^{-1} with a boundary layer thickness 100 m in a stable stratification with a Brunt–Väisälä frequency equal to 0.03 rad s^{-1}, we get $F = 3$. On a slope of 10° (if U_0 is still equal to 0.1), we therefore expect all the corrugation wavelengths larger than 60 m to be active. For both cases, the Reynolds number is so large ($Re = 10^6$ and $Re = 10^8$ for the current and the wind, respectively) that even small corrugation amplitudes (of the order of 10 % of the boundary layer thickness) generate transverse flows of the order of the mean flow (assuming Δ_c of order unity). Moreover, these flows are present in a very thin layer, which leads to strong transverse shears two orders of magnitude larger than the mean shear of the boundary layer. These shear layers are probably unstable by the Kelvin–Helmholtz instability and a non-negligible source of mixing in the boundary layer.

Acknowledgements

We would like to acknowledge U. Ehrenstein and M. Marquillie for providing the unstratified code. This work has received support from the French National Research Agency under A*MIDEX grant ANR-11-IDEX-0001-02, and is part of LABEX MEC project ANR-11-LABX-0092.

Appendix A. Small F analysis of the equation for $\tilde{w}$

In this section, we provide an asymptotic analysis of the solution to (3.8) in the limit of small F. Our objective is to obtain an estimate of the ratio $\Delta_c = |\tilde{w}_c/\tilde{w}_0|$ appearing in expression (3.17).

We assume that $\sin\alpha/(kF) = O(1)$, so that we can define the $O(1)$ parameter

$$\alpha_1 = \sin\alpha/(kF). \tag{A 1}$$

We also assume that there exists a critical point z_c (different from the wall boundary) defined by

$$U(z_c) = \alpha_1. \tag{A 2}$$

This implies that α_1 satisfies $U_{min} < \alpha_1 < U_{max}$, that is

$$\sin\alpha < kF < \frac{\sin\alpha}{U_0}. \tag{A 3}$$

A.1. *WKBJ analysis*

When $F \ll 1$, (3.8) reduces to

$$\tilde{w}'' - \left(\frac{1 - k^2F^2U^2}{F^2(\alpha_1^2 - U^2)} + O(1)\right)\tilde{w} = 0. \tag{A 4}$$

This equation is adequate for a resolution using WKBJ methods (see, for instance, Bender & Orszag 1978). Far from the critical point, the solutions can be written to leading order as

$$\tilde{w} \sim A\beta^{-1/4}\exp\left(\frac{1}{F}\int_{z_c}^{z}\sqrt{\beta}\right) + B\beta^{-1/4}\exp\left(-\frac{1}{F}\int_{z_c}^{z}\sqrt{\beta}\right), \tag{A 5}$$

where

$$\beta(z, kF) = \frac{1-(kF)^2U^2}{\alpha_1^2 - U^2(z)}. \tag{A 6}$$

Between 0 and z_c, β is positive, so the solution is of exponential type. In this interval, the solution will then be dominated by one of the exponentials. It will be convenient to write it as

$$\tilde{w} \sim \tilde{w}(0)\left(\frac{\beta(0)}{\beta}\right)^{1/4} \exp\left(-\frac{1}{F}\int_0^z \sqrt{\beta}\right). \tag{A 7}$$

By contrast, in the outer interval (z_c, z_∞), the solution is oscillatory and can be written as

$$\tilde{w}^+ \sim A(-\beta)^{-1/4} \exp\left(\frac{\mathrm{i}}{F}\int_{z_c}^z \sqrt{-\beta}\right) + B(-\beta)^{-1/4} \exp\left(-\frac{\mathrm{i}}{F}\int_{z_c}^z \sqrt{-\beta}\right). \tag{A 8}$$

If $kF < 1$, the solution is oscillatory up to infinity ($z_\infty = \infty$): it must be an outgoing wave (as required by causality) which imposes $B = 0$. If $kF > 1$, z_∞ is a finite location defined by $kFU(z_\infty) = 1$. The solution becomes evanescent again after the turning point z_∞. The condition for matching an oscillating solution and an evanescent solution across a turning point is classical (see Bender & Orszag 1978). It gives the condition

$$B = -\mathrm{i}A \exp\left(\frac{2\mathrm{i}}{F}\int_{z_c}^{z_\infty} \sqrt{-\beta}\right). \tag{A 9}$$

In the following, we write $B = K_\pm$ A where K_- and K_+ correspond to the constant when $kF < 1$ and $kF > 1$ respectively. We do not consider the special case $kF = 1$ for which the turning point is at infinity.

The WKBJ approximations are not valid close to z_c. If $F^2Re^{1/3} \gg 1$, the region $|z - z_c| = O(F^2)$ is far away from the critical layer. In this region, $\tilde{w}$ is still given by (A 4) which to leading order now reduces to

$$\tilde{w}'' + \left(\frac{\cos^2\alpha}{2F^2\alpha_1 U_c'(z-z_c)}\right)\tilde{w} = 0. \tag{A 10}$$

This equation admits the general solutions

$$\tilde{w} = a^+\sqrt{\tilde{z}}\mathrm{J}_1(\sqrt{\tilde{z}}) + b^+\sqrt{\tilde{z}}Y_1(\sqrt{\tilde{z}}), \quad \text{for } \tilde{z} > 0, \tag{A 11a}$$

$$\tilde{w} = a^-\sqrt{-\tilde{z}}\mathrm{I}_1(\sqrt{-\tilde{z}}) + b^-\sqrt{-\tilde{z}}\mathrm{K}_1(\sqrt{-\tilde{z}}), \quad \text{for } \tilde{z} < 0, \tag{A 11b}$$

where

$$\tilde{z} = \frac{2\cos^2\alpha}{F^2\alpha_1 U_c'}(z - z_c). \tag{A 12}$$

Matching with the WKBJ approximations requires

$$a^- = \frac{\sqrt{2\pi\alpha_1 U_c' F}}{\cos\alpha(\alpha_1^2 - U_0^2)^{1/4}}\tilde{w}(0)\exp\left(-\frac{1}{F}\int_0^{z_c}\sqrt{\beta}\right), \tag{A 13a}$$

$$a^+ = \frac{\sqrt{2\pi\alpha_1 U_c' F}}{2\cos\alpha}\mathrm{e}^{3\mathrm{i}\pi/4}(1 + \mathrm{i}K_\pm)A, \tag{A 13b}$$

$$b^+ = \frac{\sqrt{2\pi\alpha_1 U_c' F}}{2\cos\alpha} \mathrm{e}^{-3\mathrm{i}\pi/4}(1 - \mathrm{i}K_\pm)A. \tag{A 13c}$$

The solutions (A 11*a*,*b*) are not regular at z_c. Close to z_c, (A 11*a*,*b*) has the expansions

$$\tilde{w} \sim a^+ \frac{\tilde{z}}{2} - \frac{2b^+}{\pi}\left(1 - \frac{\tilde{z}(\ln(\tilde{z}) - 2\ln(2) - 1 + 2\gamma)}{4}\right), \quad \text{for } \tilde{z} > 0, \tag{A 14a}$$

$$\tilde{w} \sim -a^- \frac{\tilde{z}}{2} + b^-\left(1 - \frac{\tilde{z}(\ln(-\tilde{z}) - 2\ln(2) - 1 + 2\gamma)}{4}\right), \quad \text{for } \tilde{z} < 0. \tag{A 14b}$$

This critical layer singularity can only be smoothed by introducing viscous effects. However, this is not necessary for obtaining the relations between a^-, b^- and a^+, b^+. Indeed, when $F^2 Re^{1/3} \gg 1$, the solution is expected to remain regular on a contour that avoids the singularity in the lower complex $\tilde{z}$-plane. This condition means that (A 14*b*) should correspond to (A 14*a*) where $-\tilde{z}$ has been changed into $\tilde{z}\mathrm{e}^{-\mathrm{i}\pi}$ in the logarithm. This yields the following conditions:

$$b^- = -\frac{2}{\pi} b^+, \tag{A 15a}$$

$$a^- + a^+ = -\frac{\mathrm{i}\pi}{2} b^-. \tag{A 15b}$$

Note that these conditions could have been directly obtained by requiring (A 11*a*) to be valid for $-\pi \leqslant \arg(\tilde{z}) \leqslant 0$. This would have implied that (A 11*a*) is valid for negative $\tilde{z}$ with $\sqrt{\tilde{z}}$ defined as $-\mathrm{i}\sqrt{-\tilde{z}}$ for negative $\tilde{z}$. The equations (A 13*a*–*c*) and (A 15*a*,*b*) give a relation between $\tilde{w}(0)$ and $\tilde{w}(z_c) = b^-$ which can be written as

$$\tilde{w}(z_c) = \tilde{w}(0) K_{o\pm} \sqrt{F} \exp\left(-\frac{1}{F}\int_0^{z_c} \sqrt{\beta}\right), \tag{A 16}$$

where $K_{o\pm}$ is a constant independent of F:

$$K_{o\pm} = \frac{(1 - \mathrm{i}K_\pm)\sqrt{2\pi\alpha_1 U_c'}}{\pi(\alpha_1^2 - U_0^2)^{1/4}\cos\alpha} \mathrm{e}^{\mathrm{i}\pi/4}. \tag{A 17}$$

Expression (A 16) demonstrates that $|\tilde{w}_c/\tilde{w}_0|$ is in general exponentially small. There is an important exception which occurs when z_c is close to the wall.

A.2. *Special case of the critical point close to the wall*

We shall see that large values of $|\tilde{w}_c/\tilde{w}_0|$ can be obtained when $z_c = O(F^2)$. This condition requires that $\alpha_1 - U_0 = O(F^2)$, so that

$$z_c \approx (\alpha_1 - U_0)/U_0' = (\alpha_1 - U_0)/(1 - U_0^2). \tag{A 18}$$

The local solution is then valid between 0 and z_c and can be written for $\tilde{z} < 0$ as

$$\tilde{w} = (1 + \mathrm{i}K_\pm)\sqrt{-\tilde{z}}\mathrm{J}_1(-\mathrm{i}\sqrt{-\tilde{z}}) + \mathrm{i}(1 - \mathrm{i}K_\pm)\sqrt{-\tilde{z}}Y_1(-\mathrm{i}\sqrt{-\tilde{z}}). \tag{A 19}$$

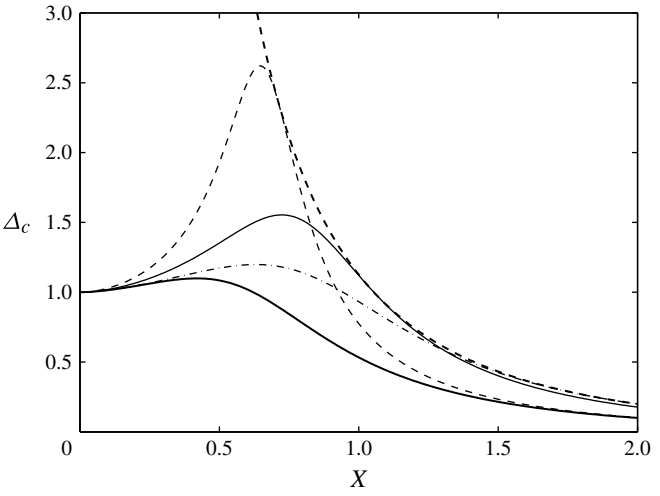

FIGURE 12. The function $\Delta_c = |\tilde{w}(\tilde{z}_c)/\tilde{w}(0)|$ versus X. The thick solid line is $\Delta_c^-(X)$, for $kF < 1$. The thick dashed line is $\Delta_{c\,max}^+(X)$ (maximum value of Δ_c^+ over all Φ for $kF > 1$). The thin lines are Δ_c^+ for $\Phi = \pi/2$ (dash-dotted), $\Phi = 2\pi/3$ (solid) and $\Phi = 5\pi/6$ (dashed).

Therefore the ratio $\Delta_c = |\tilde{w}(\tilde{z}_c)/\tilde{w}(0)|$ satisfies

$$\Delta_c^- = \frac{2}{\pi X\,|\mathrm{J}_1(-\mathrm{i}X) + \mathrm{i}Y_1(-\mathrm{i}X)|} \quad \text{when } kF < 1, \tag{A 20a}$$

$$\Delta_c^+ = \frac{2}{\pi X\,|\mathrm{J}_1(-\mathrm{i}X)/\tan\Phi + Y_1(-\mathrm{i}X)|} \quad \text{when } kF > 1, \tag{A 20b}$$

where

$$\Phi = \frac{1}{F}\int_{z_c}^{z_\infty} \sqrt{-\beta}, \tag{A 21a}$$

$$X = \sqrt{-\tilde{z}_c} = \sqrt{\frac{2(\alpha_1 - U_0)\cos^2\alpha}{(1-U_0^2)^2F^2\alpha_1}}. \tag{A 21b}$$

The functions $\Delta_c^\pm$ can also be written as

$$\Delta_c^- = \frac{1}{X\sqrt{[\mathrm{K}_1(X)]^2 + \pi^2[\mathrm{I}_1(X)]^2}}, \tag{A 22a}$$

$$\Delta_c^+ = \frac{1}{X\sqrt{\left[\mathrm{K}_1(X) + \dfrac{\pi}{2\tan\Phi}\mathrm{I}_1(X)\right]^2 + \dfrac{\pi^2}{4}[\mathrm{I}_1(X)]^2}}. \tag{A 22b}$$

When $kF < 1$, the maximum of Δ_c^- is $\Delta_{c\,max}^- \approx 1.1$, attained for $X \approx 0.42$; when $kF > 1$, the maximum of Δ_c is not bounded. For a fixed X, its maximum value, attained when

$$\tan\Phi_{max} = -\frac{\pi}{2}\frac{\mathrm{I}_1(X)}{\mathrm{K}_1(X)}, \tag{A 23}$$

is

$$\Delta_{c\,max}^{+}(X) = \frac{2}{\pi X \mathrm{I}_1(X)}. \tag{A 24}$$

This maximum diverges as $4/(\pi X^2)$ for small X. For a fixed Φ, Δ_c^+ exhibits a maximum for a value X^{max} smaller than 0.73. This maximum is largest when Φ is slightly below a multiple of π. In that case, X^{max} is very close to 0. In contrast, when Φ is exactly equal to a multiple of π, the function Δ_c^+ vanishes for all $X > 0$.

The function Δ_c is plotted for both $kF < 1$ and $kF > 1$ in figure 12.

REFERENCES

ABRAMOWITZ, M. & STEGUN, I. A. 1965 *Handbook of Mathematical Functions*. Dover.

ACHESON, D. J. 1976 On over-reflection. *J. Fluid Mech.* **77**, 433–472.

ATHANASSIADOU, M. & CASTRO, I. P. 2001 Neutral flow over a series of rough hills: a laboratory experiment. *Boundary-Layer Meteorol.* **101**, 1–30.

BAI, Y. 2012 Rayonnement d'une couche limite dans un milieu stratifié. Master's thesis, University Paris XI.

BENDER, C. M. & ORSZAG, S. A. 1978 *Advanced Mathematical Methods for Scientists and Engineers*. McGraw-Hill.

BENNEY, D. J. & BERGERON, R. F. 1969 A new class of nonlinear waves in parallel flows. *Stud. Appl. Maths* **48**, 181–204.

BESIO, G., BLONDEAUX, P., BROCCHINI, M. & VITTORI, G. 2004 On the modeling of sand wave migration. *J. Geophys. Res.* **109**, 1–13.

BOULANGER, N., MEUNIER, P. & LE DIZÈS, S. 2007 Structure of a tilted stratified vortex. *J. Fluid Mech.* **583**, 443–458.

BOULANGER, N., MEUNIER, P. & LE DIZÈS, S. 2008 Instability of a tilted vortex in stratified fluid. *J. Fluid Mech.* **596**, 1–20.

CANDELIER, J., LE DIZÈS, S. & MILLET, C. 2012 Inviscid instability of a stably stratified compressible boundary layer on an inclined surface. *J. Fluid Mech.* **694**, 524–539.

DRAZIN, P. G. & REID, W. H. 1981 *Hydrodynamic Stability*. Cambridge University Press.

FINNIGAN, J. J., SHAW, R. H. & PATTON, E. G. 2009 Turbulence structure above a vegetation canopy. *J. Fluid Mech.* **637**, 387–424.

FREHLICH, R., MEILLIER, Y. & JENSEN, M. L. 2008 Measurements of boundary layer profiles with *in situ* sensors and doppler lidar. *J. Atmos. Ocean. Technol.* **25**, 1328–1340.

GARRATT, J. 1992 *The Atmospheric Boundary Layer*. Cambridge University Press.

GARRETT, C., MACCREADY, P. & RHINES, P. 1993 Boundary mixing and arrested Ekman layers: rotating stratified flow near a sloping boundary. *Annu. Rev. Fluid Mech.* **25**, 291–323.

GENIN, A., DAYTON, P. K., LONSDALE, P. F. & SPIESS, F. N. 1986 Corals on seamount peaks provide evidence of current acceleration over deep sea topography. *Nature* **322**, 59–61.

GONG, W., TAYLOR, P. A. & DORNBRACK, A. 1996 Turbulent boundary-layer flow over fixed aerodynamically rough two-dimensional sinusoidal waves. *J. Fluid Mech.* **312**, 1–31.

HABERMAN, R. 1972 Critical layers in parallel flows. *Stud. Appl. Maths* **51**, 139–161.

JACKSON, S. & HUNT, J. C. R. 1975 Turbulent wind flow over a low hill. *Q. J. R. Meteorol. Soc.* **101**, 929–955.

LIN, C. C. 1955 *The Theory of Hydrodynamic Stability*. Cambridge University Press.

LINDZEN, R. S. & BARKER, J. W. 1985 Instability and wave over-reflection in stably stratified shear flow. *J. Fluid Mech.* **151**, 189–217.

MACCREADY, P. & PAWLAK, G. 2001 Stratified flow along a rough slope: separation drag and wave drag. *J. Phys. Oceanogr.* **31**, 2824–2839.

MAHRT, L. 2014 Stably stratified atmospheric boundary layers. *Annu. Rev. Fluid Mech.* **46**, 23–45.

MARQUILLIE, M. & EHRENSTEIN, U. 2002 Numerical simulation of a separating boundary-layer flow. *Comput. Fluids* **31**, 683–693.

MARQUILLIE, M. & EHRENSTEIN, U. 2003 On the onset of nonlinear oscillations in a separating boundary-layer flow. *J. Fluid Mech.* **490**, 169–188.

NADEAU, D. F., PARDYJAK, E. R., HIGGINS, C. W. & PARLANGE, M. B. 2013 Similarity scaling over a steep alpine slope. *Boundary-Layer Meteorol.* **147**, 401–419.

OHYA, Y. 2001 Wind-tunnel study of atmospheric stable boundary layers over a rough surface. *Boundary-Layer Meteorol.* **98**, 57–82.

OHYA, Y. & UCHIDA, T. 2008 Laboratory and numerical studies of the atmospheric stable boundary layers. *J. Wind Engng Ind. Aerodyn.* **96**, 2150–2160.

PARK, M. S. & PARK, S. U. 2006 Effects of topographical slope angle and atmospheric stratification on surface-layer turbulence. *Boundary-Layer Meteorol.* **147**, 613–633.

PASSAGGIA, P.-Y., LEWEKE, T. & EHRENSTEIN, U. 2012 Transverse instability and low-frequency flapping in separated boundary-layer flows: an experimental study. *J. Fluid Mech.* **703**, 363–373.

RIEDINGER, X., LE DIZÈS, S. & MEUNIER, P. 2011 Radiative instability of the flow around a rotating cylinder in a stratified fluid. *J. Fluid Mech.* **672**, 130–146.

SARIC, W. S., REED, H. L. & KERSCHEN, E. J. 2002 Boundary-layer receptivity to freestream disturbances. *Annu. Rev. Fluid Mech.* **34**, 291–319.

SYKES, R. I. 1978 Stratification effects in boundary layer flow over hills. *Proc. R. Soc. Lond.* A **361**, 225–243.

TAYLOR, P. A., MASON, P. J. & BRADLEY, E. F. 1987 Boundary-layer flow over low hills. *Boundary-Layer Meteorol.* **39**, 107–132.

THORPE, S. A. 1992 The generation of internal waves by flow over the rough topography of a continental slope. *Proc. R. Soc. Lond.* A **439**, 115–130.

VAN HAREN, H. & HOWARTH, M. J. 2004 Enhanced stability during reduction of stratification in the north sea. *Cont. Shelf Res.* **24**, 805–819.

WU, X. & ZHANG, J. 2008*a* Instability of a stratified boundary layer and its coupling with internal gravity waves. Part 1. Linear and nonlinear instabilities. *J. Fluid Mech.* **595**, 379–408.

WU, X. & ZHANG, J. 2008*b* Instability of a stratified boundary layer and its coupling with internal gravity waves. Part 2. Coupling with internal gravity waves via topography. *J. Fluid Mech.* **595**, 409–433.